
1
2 This pre-print has been submitted as a manuscript for publication in the BULLETIN OF THE
3 SEISMOLOGICAL SOCIETY OF AMERICA. Please note that, despite having undergone peer-
4 review, the manuscript has yet to be formally accepted for publication. Subsequent versions of this
5 pre-print may have slightly different content. If accepted, the final version will be available via the
6 'Peer-reviewed Publication DOI' link on the right-hand side of this webpage. Please feel free to
7 contact any of the authors; we welcome feedback

9 A probabilistic displacement hazard assessment framework for
10 distributed ruptures from strike-slip earthquakes

11 Alba M. Rodriguez Padilla ^{*1} and Michael E. Oskin¹

12 ¹*Department of Earth and Planetary Sciences, University of California, Davis*

13 **Abstract**

14 Widespread distributed fracturing during earthquakes threatens infrastructure and lifelines.
15 We combine high-resolution rupture maps from the five major surface-rupturing strike-slip earth-
16 quakes in southern California and northern Mexico since 1992 to incorporate the displacements
17 produced by secondary ruptures into a probabilistic displacement hazard analysis framework.
18 Through analysis of the spatial distribution of mapped ruptures and displacements for each of
19 these events, we develop a magnitude-dependent expression for the probability per unit area
20 of finding a secondary rupture that accommodates a displacement that exceeds a displacement
21 threshold at a given distance away from the principal fault. Our model is best applied to esti-
22 mating expected secondary displacements for strike-slip earthquakes, similar to those analyzed,
23 with widespread ruptures across immature fault zones.

24 **Key points**

- 25 1. Strike-slip earthquakes on immature faults cause widespread ruptures that can threaten in-
26 frastructure.
- 27 2. We present a probabilistic fault displacement hazard model based on high-resolution surface
28 rupture maps and displacement measurements.
- 29 3. Our model may be used to estimate secondary rupture displacements for strike-slip events on
30 immature faults.

31 **Introduction**

32 Displacements from surface-rupturing earthquakes directly threaten infrastructure and lifelines in
33 tectonically active regions. Probabilistic fault displacement hazard analysis (PFDHA) addresses this
34 challenge by providing estimates of the likelihood and distribution of surface displacements during
35 fault rupture (e.g. Youngs et al., 2003; Petersen et al., 2011; Moss and Ross, 2011; Nurminen et al.,
36 2020; Wang and Goulet, 2021). Over the past few years, earth scientists and engineers have joined
37 efforts in standardizing fault displacement hazard models from empirical measurements collected
38 after earthquakes (Baize et al., 2016; Baize et al., 2020; Sarmiento et al., 2021). The data these

*Corresponding author. arodriguezpadilla@ucdavis.edu

39 efforts are based on has improved due to increased coverage of surface rupturing earthquakes (e.g.
40 airborne lidar, Chen et al., 2015; Hudnut et al., 2020), better post-earthquake response coordination
41 (e.g. Mattioli et al., 2020), and advances in the repeat frequency and resolution of geodetic methods
42 (e.g. Milliner and Donnellan, 2019; Xu et al., 2020).

43 We present a fault displacement model focused on distributed ruptures for strike-slip faults using data
44 from five major surface rupturing earthquakes in the Eastern California Shear Zone and Northern
45 Mexico. These events left behind impressive footprints of broadly distributed ruptures in the desert
46 that have been carefully mapped: the Landers (1992), Hector Mine (1999), El Mayor-Cucapah
47 (2010), and Ridgecrest (2019 foreshock and mainshock) earthquakes (Sieh et al., 1993; Lazarte et
48 al., 1994; Treiman et al., 2002; Hudnut et al., 2002; Fletcher et al., 2014; Teran et al., 2015; Milliner
49 et al., 2015; Milliner et al., 2016; Ponti et al., 2020; DuRoss et al., 2020; Rodriguez Padilla et
50 al., 2022a). The hazard posed by secondary ruptures remains poorly characterized, challenging the
51 ability of engineers and other stakeholders to evaluate the associated risk. In this contribution, we
52 use surface rupture maps and displacement measurements from these well-documented earthquakes
53 to fill this information gap. To do so, we develop a relationship for the probability per unit area of
54 finding a rupture at a distance away from the principal fault that will have a displacement greater
55 than a threshold. This relationship may be used by end-users to quantify surface displacement hazard
56 in a probabilistic framework that can inform the design and evaluation of lifelines and engineered
57 structures located near or across active fault zones.

58 1 Surface rupture and displacement measurements

59 The Fault Displacement Hazard Initiative (FDHI) database, hosted and maintained by the Natural
60 Hazards Risk & Resilience Research Center at the University of California, Los Angeles, includes
61 66 surface-rupturing earthquakes, with moment magnitudes ranging from 5.0 to 8.0, of all faulting
62 styles (Sarmiento et al., 2021). The database incorporates surface rupture maps and displacement
63 measurements for each of the events. The ruptures are classified as primary and distributed. The
64 slip measurements document magnitude and location, and, sometimes, direction.

65 We select five strike-slip events from the FDHI rupture database, the 1992 M_w 7.3 Landers, 1999 M_w
66 7.1 Hector Mine, 2010 M_w 7.2 El Mayor-Cucapah, and 2019 Ridgecrest earthquakes (separated into
67 M_w 6.4 foreshock and M_w 7.1 mainshock; Figure 1) to incorporate into our model. We choose these
68 events because they are well-mapped, and they occurred on relatively immature faults (< 25 km
69 cumulative displacement) that share the same regional tectonic setting (Eastern California Shear
70 Zone and northern Baja California transtensional rift).

71 The surface rupture maps in the FDHI database include some variability in completeness and map-
72 ping style. Overall, the near-field section of these earthquakes (<1 km from the principal rupture
73 trace) is mapped at a similar resolution, while the far-field has some variability in spatial complete-
74 ness and resolution. Specifically, the rupture map for the El Mayor-Cucapah earthquake includes
75 ruptures mapped from radar data at its northern end into southern California and its southern end
76 through the Colorado River Delta (Figure 1)(Fletcher et al., 2014). We remove these radar-based
77 features, which are mapped more simply than the field and lidar-based ruptures, and thus induce a
78 biased population of long ruptures that increase far-field rupture density unrealistically. Similarly,
79 the foreshock and mainshock Ridgecrest maps contain some features that are doubly mapped, of
80 which we remove the simplified traces (Ponti et al., 2020; DuRoss et al., 2020).

A displacement model for secondary ruptures from surface rupture and displacement maps

We define probabilistic fault displacement hazard as the probability per unit area of finding a rupture at a distance x away from the principal fault with slip greater than a threshold S_0 . Computing this probability requires knowledge of the spatial distribution of ruptures and the displacements that these ruptures could accommodate. We address the former through analysis of the distribution of rupture density and the latter by examining the distribution of surface displacements measured for each of our selected events. The fault displacement hazard results from the joint probability,

$$\begin{aligned} P(S > S_0|x, M_w) &= P(\text{rupture}|x) \\ &P(S > S_0|x, \text{rupture}, M_w), \end{aligned} \quad (1)$$

where $P(S > S_0|x, M_w)$ is the probability per unit area of finding a rupture at a distance away from the fault, resulting from an event of a given magnitude, that will have a displacement greater than the threshold S_0 . $P(\text{rupture}|x)$ is the probability of rupture per unit area occurring at that location. $P(S > S_0|x, \text{rupture}, M_w)$ is the displacement exceedance, a probability of finding a displacement that exceeds that threshold at a given distance from the fault, given the presence of a rupture, for a given earthquake magnitude. Note that in fitting the second term in equation 1, we assume that all of the measured surficial displacements in the FDHI database are associated with discrete fault ruptures and not produced by other mechanisms, such as ground failure.

To assess the probability of observing a rupture (first term in equation 1), we use the surface rupture maps in the FDHI database. The probability of observing a rupture at a given distance away from the fault can be obtained from the spatial distribution of fracture density (e.g. Rodriguez Padilla et al., 2022b), which is given by the inverse power-law:

$$\nu(x) = \nu_o \left(\frac{x + x_f}{x_f} \right)^{-\gamma} \quad (2)$$

Where ν_o is the rupture density at the origin in number of ruptures per unit $1m^2$ area, x_f is a normalizing constant and related to the uncertainty of the location of the fault trace in meters (Rodriguez Padilla et al., 2022b) The exponent γ is the slope of the decay of rupture density with distance in log-log space, or scaling exponent. $\nu(x)$ is the probability of a rupture occurrence per unit $1m^2$ area.

We use equation 2 to calculate the rupture density distribution (and thus the probability of finding a rupture per unit area) for the Landers, Hector Mine, and El Mayor-Cucapah earthquakes (Figure 2). To do this, we discretize individual ruptures into 1-meter spaced points so that mapping choices do not bias the rupture density estimates (Rodriguez Padilla et al., 2022b). The principal rupture trace for each event (i.e. the fault with respect to which fault-perpendicular distance is measured) is simplified from the ruptures mapped as primary in each of the rupture maps in the FDHI rupture database (figure A1 in the appendix), with the exception of the Ridgecrest mainshock where a second fault in the middle of the dry lake bed was added based on the mapping of Rodriguez Padilla et al. (2022b). We fit each parameter in equation 2 to the rupture data using an ensemble sampler Monte Carlo Markov Chain (see supplementary methods section). The maximum likelihood fits and posterior distributions for x_{fr} and γ are shown in figure 2 and provided in table 1. Note that the rupture distributions are independent of earthquake magnitude, with all events having similar rupture densities ν_o at the fault, hence the magnitude-independence of the first term in equation 1.

119 To assess displacement exceedance (second term in equation 1), we include only the displacements
120 in the FDHI database (supplementary figure A2) measured in the field, and exclude measurements
121 derived from other techniques, such as image correlation. This is to ensure that the displacement
122 measurements we consider are collected over apertures consistent with the width of individual rup-
123 tures. The vast majority of the displacements in the database are lateral and therefore record
124 shear, with a minor portion of them recorded in absolute terms, where both lateral and vertical
125 displacements are recorded as a ratio, representing a mixed-mode fracture. Because of the lim-
126 ited information available on fracture mode and displacement direction, our models are constructed
127 without consideration of these parameters.
128 Coseismic displacements are highest along the principal fault trace and decline to lower values on
129 distributed ruptures. We find that the mean values of displacement measurements from the FDHI
130 database, binned with respect to distance to the principal fault trace, may be modeled as an inverse
131 power-law described by:

$$\lambda(x) = \beta \left(\frac{x + x_S}{x_S} \right)^{-n} \quad (3)$$

132 where λ is the mean of the displacement at every distance bin, β is the average displacement
133 at the origin, x is the location away from the principal fault trace, x_S is a normalization factor
134 held constant at 1 meter (see supplementary methods in the appendix), and n is the slope of the
135 relationship between mean displacement and distance in log-log space, or the scaling exponent.
136 We fit equation 3 to the distribution of average displacements with distance for each of the events
137 using an ensemble sampler for Monte-Carlo Markov Chain (see appendix for detailed method). The
138 maximum likelihood fits and posterior distributions for β and n are shown in figure 3 and provided
139 in table 1. Values of β range from 1.2 meters for the Ridgecrest foreshock to 4.4 meters for the
140 Hector Mine event, broadly consistent with the average slip at the fault in each earthquake.

141 We find that the values of n agree between the different events, averaging around 0.45, though the
142 fits vary in quality between events, with the Ridgecrest foreshock and the Hector Mine events being
143 the least well characterized by equation 3. This poor characterization arises from the broader zone of
144 similar average displacement measurements near the principal fault trace, and much higher scatter
145 in the further (< 1 km from the fault in Hector Mine and < 100 m from the fault in the Ridgecrest
146 foreshock) displacements measured in the field (Figure 3). This is clear in the residuals of the fit
147 of 3 to the field displacement data from these two events (figure A5 in the appendix). In the case
148 of the Ridgecrest foreshock, the constant average displacement values near the intercept may arise
149 from incomplete rupture to the surface, which may be a magnitude-dependent characteristic. This
150 is something we do not consider in our model.

151 The scaling exponent, n , that describes the spatial distribution of mean displacement is very con-
152 sistent for the Ridgecrest mainshock, the Landers, and the El Mayor-Cucapah events, and these
153 events exhibit low residuals for the fit of equation 3 to the field displacement data (figure A5 in the
154 appendix).

155 Within each distance bin, we find that the population of field displacement measurements is well
156 described by an exponential distribution (Figure 4). This relationship holds up remarkably well for
157 all of the distance bins analyzed, as shown by the observation of similar values for the mean and the
158 standard deviation of displacement measurements within each bin (supplementary figure A3). The
159 distribution of displacements within a distance bin can thus be described as follows:

$$f(S|x) = \frac{1}{\lambda} e^{-\frac{S}{\lambda}} \quad (4)$$

160 where λ , the mean of the displacement at every distance bin, is the output of equation 3. Combining
 161 equations 3 and 4 yields:

$$f(S) = \frac{1}{\beta} \left(\frac{x + x_S}{x_S} \right)^n e^{-\frac{S}{\beta} \left(\frac{x + x_S}{x_S} \right)^n} \quad (5)$$

162 Equation 5 is a probability density function (PDF) of observed displacements with distance from
 163 the principal fault trace. We integrate this PDF from S_0 , the threshold displacement of interest,
 164 to S_{max} , the maximum observed slip in an event (note that we expect $S_{max} \geq \beta$), to solve for the
 165 probability of observing a displacement that exceeds S_0 on an observed rupture given an earthquake
 166 magnitude (second term of equation 1):

$$\begin{aligned} P(S > S_0 | x, rupture, M_w) &= \int_{S_0}^{S_{max}} \frac{1}{\beta} \left(\frac{x + x_S}{x_S} \right)^n \\ &\quad e^{-\frac{S}{\beta} \left(\frac{x + x_S}{x_S} \right)^n} dS \\ &= -e^{-\frac{S}{\beta} \left(\frac{x + x_S}{x_S} \right)^n} \Big|_{S_0}^{S_{max}} \end{aligned} \quad (6)$$

167 Note that in evaluating this integral, the term containing S_{max} is small, so that as long as $S_0 \ll$
 168 S_{max} , this term can be ignored. This limits the appropriate application of our model to predicting
 169 the probability of secondary displacements above a threshold that is a fraction (i.e. 10%) of the
 170 slip measured on the primary fault trace. This limitation is appropriate because solving only for
 171 the probability of large slip values would be akin to predicting the presence of another primary
 172 fault trace, which is not the objective of this model. With this application in mind, completing the
 173 integration of equation 6 yields:

$$P(S > S_0 | x, rupture, M_w) = e^{-\frac{S_0}{\beta} \left(\frac{x + x_S}{x_S} \right)^n} \quad (7)$$

174 The displacement threshold, S_0 , may be adjusted by end-users for different engineering applications.
 175 Combining the probabilities in equations 2 and 7 yields the solution to equation 1:

$$P(S > S_0 | x, M_w) = \nu_o \left(\frac{x + x_f}{x_f} \right)^{-\gamma} e^{-\frac{S_0}{\beta} \left(\frac{x + x_S}{x_S} \right)^n} \quad (8)$$

176 Note that the magnitude-dependence in this model arises from parameter β , the average displacement
 177 on the fault.

178 Figure 5 shows the relationship in equation 8 for each dataset for $x=1$ to $x=10$ kilometers away
 179 from the fault, consistent with the extent of ruptures shown in Figure 2, with example values of S_0
 180 of 0.01, 0.1, and 0.5 meters. The probabilities of finding a rupture that hosts displacements larger
 181 than 1 mm near the fault exceed 10% for all of the events considered here, reaching 20% for the
 182 Ridgecrest foreshock (Figure 5, left). Despite the smaller magnitude, the Ridgecrest foreshock has
 183 the highest rupture density at the fault, which results in higher probabilities $P(S > S_0)$, despite the
 184 lower value of β , at this displacement threshold. $P(S > S_0)$ decreases rapidly with distance for all
 185 events, even for this small value of S_0 , such that the probability of finding a rupture that hosts a
 186 displacement larger than 1 mm is lower than 1 in 1,000 beyond 10 km from the primary fault trace.

187 The surface rupture hazard curves for the Ridgecrest mainshock, Landers, El Mayor-Cucapah, and
188 Hector Mine events look very similar for $S_0 = 1$ cm to those for $S_0 = 1$ mm. The variability of
189 $P(S > S_0)$, about a factor of 2, at the intercept, arises largely from the variability in rupture density
190 for the different events and likely reflects the natural variability that may be expected for these
191 events and low displacement thresholds, regardless of magnitude (Figure 5, center). The magnitude-
192 dependence of the model becomes clear with increasing distance away from the fault, given by the
193 larger slope of $P(S > S_0)$ for the smaller-magnitude Ridgecrest foreshock. This pattern becomes
194 even more obvious for the $P(S > S_0)$ curves where $S_0 = 0.5$ meters (Figure 5, right). At this
195 displacement threshold, the effect of magnitude, captured by parameter β , trumps that of rupture
196 density at the intercept and the Ridgecrest foreshock has a lower probability of finding a rupture
197 hosting a displacement larger than 0.5 meters than that of the mainshock or Landers. When $S_0 = 0.5$
198 m, $P(S > S_0)$ becomes lower than 1 in 10,000 at about 1 km away from the fault for the Ridgecrest
199 mainshock, the Landers, the Hector Mine, and the El Mayor-Cucapah events. This hazard level is
200 crossed at about 200 m from the fault for the Ridgecrest foreshock.

201 A generalized rupture-displacement probability model

202 The individual models of $P(S > S_0)$ for each event (figure 5) can be used to inform a general model
203 that is representative of events like these, i.e., those dominated by distributed deformation, largely
204 rupturing through sediment, hosted on immature fault zones.

205 To estimate the first term of $P(S > S_0)$ for the general model, which is independent of earthquake
206 magnitude, we combine the rupture distributions from the FDHI database from these five earth-
207 quakes and estimate a general relationship for rupture density with fault-perpendicular distance
208 using equation 2 (figure A4 in the appendix). This is possible because the parameters describing the
209 spatial distributions of rupture density for all events overlap within error, irrespective of magnitude
210 or other event characteristics.

211 The second term in $P(S > S_0)$ is magnitude-dependent and therefore requires more careful exami-
212 nation to be generalized. The scaling exponent, n , that describes the spatial distribution of mean
213 displacement is very consistent for the M_w 7.1 Ridgecrest mainshock, the M_w 7.3 Landers, and the
214 M_w 7.2 El Mayor-Cucapah events, and the distribution of field displacements for these events is well
215 described by equation 3, as captured by the low residuals (figure A5 in the appendix). Thus, to
216 estimate n in our general model, we combine the posterior distributions of n from the Landers, El
217 Mayor-Cucapah, and Ridgecrest mainshock displacement distributions (figure A6 in the appendix).
218 We find that n is normally distributed with a mean value of 0.44 and a standard deviation of 0.08.
219 The magnitude-dependence of our probabilistic displacement model arises from parameter β , which
220 we propose may be estimated using the empirical relationship for average displacement as a function
221 of magnitude from Brengman et al. (2019):

$$\beta = 10^{\frac{M_w - a}{b}} \quad (9)$$

222 where $a = 6.5197 \pm 0.131$ and $b = 1.0824 \pm 0.2323$ are the regression coefficients determined by
223 Brengman et al. (2019) for strike-slip earthquakes.

224 Two examples of the general model are shown in Figure 6. One for events of $M_w = 6, 6.5, 7$ and 7.5 ,
225 all with $S_0 = 0.1$ m (Figure 6, left), and a second for values of $S_0 = 0.01, 0.1, 0.5$, and 1 m for an M_w 7
226 event (Figure 6, right). The magnitude dependence of $P(S > S_0)$ for a fixed displacement threshold
227 S_0 manifests as an increasingly wider hazard envelope, i.e. slope and intercept increase proportionally
228 with magnitude. For a fixed magnitude, the slope describing the probability $P(S > S_0)$ decreases
229 with increasing displacement threshold S_0 , and the intercept increases with decreasing values of S_0 .

Parameter error estimates

The parameters that build our probabilistic displacement model $P(S > S_0)$ have uncertainties that must be accounted for. The sources of uncertainty in the model are the fitting error in the exponent n that describes the PDF of displacements for an event, the uncertainty in the average displacement at the fault, β , which combines the errors in parameters a and b from equation 9 (Bregman et al., 2019), and the uncertainty in the fits to x_{fr} , v_o , and γ which describe the spatial distribution of rupture density.

To combine the errors in both terms in equation 8, we make a prediction for $P(S > S_0)$ under each set of samples from our suite of 5000 combined parameter sets. The parameters in the first term of equation 8, which describe the spatial distribution of rupture density, are correlated, so they must be sampled from the same state of the Markov chain for this correlation to be preserved. The parameters in the displacement term in equation 8 are normally distributed. To consider the variability of n and β (a and b) in our uncertainty estimates, we draw random samples from a normal distribution where the best fit of each parameter is the mean and the standard deviation is the standard error of n for a and b reported in Bregman et al. (2019), and the standard deviation of n as calculated here (figure A6 in the appendix).

A general model with $S_0 = 0.1$ m and M_w 7, with uncertainties, as well as the model residuals resulting from the 5000 iterations of Monte Carlo sampling are shown in figure 7. The uncertainty distributions of each parameter are shown in figure A7 in the appendix. The incompleteness of the rupture maps in the far field contributes to the conical shape of the uncertainty distribution, which is largely inherited from the uncertainty in the rupture density and average displacement scaling exponents, γ and n . We estimate the one standard error by estimating the envelope of model fits at the 16th and 84th percentiles (1σ). Based on these envelopes, we expect variability in probability below one order of magnitude for $P(S > S_0)$ within 3 kilometers of the fault, increasing to 1.5 orders of magnitude at 10 km away from the fault. The standard error can be described by the expression:

$$\sigma_M = \tau e^{x^{0.15}} \quad (10)$$

where $\tau \approx 3 \times 10^{-2}$ for the 84% percentile and $\tau \approx -4 \times 10^{-2}$ for the 16% percentile. The fits of equation 10 to the model fits are shown in Figure 7 (bottom).

We provide a Jupyter Notebook (see data and resources) that allows end-users to generate their own model for $P(S > S_0)$. The only inputs required are a displacement threshold S_0 and an earthquake moment magnitude (M_w). The model outputs $P(S > S_0)$ curves with a best-fit model and an analytically defined uncertainty range using 10.

Model discussion and limitations

The model we develop in this contribution uses input rupture maps and field displacement measurements from select events in the Eastern California Shear Zone and northern Baja California. From our limited number of available surface rupturing events with high-resolution maps, there arises some challenges and assumptions in this model that limit its application. The events we cover here span the M_w 6.4-7.3 range. Within this range, we find that, surprisingly, the distribution of rupture density is not magnitude-dependent. However, this could change with an expanded dataset of high-resolution maps from more events. We find that with the data available that the secondary rupture densities at the principal fault vary by less than a factor of 10. The rupture density variability documented by Rodriguez Padilla et al. (2022b) between different portions of the Ridgcrest 2019 surface

271 ruptures, which they found to be independent of the displacement magnitude at the surface, exceeds
272 this level of variability. Hence there is no basis at this time to develop a magnitude-dependent
273 estimator of secondary rupture density.

274 The magnitude-dependence in the models for individual events and for our general model arises from
275 parameter β , the expected average displacement measured at the primary fault. This parameter
276 separates the Ridgecrest foreshock from the other events distinctly. For the other, M_w 7.1 to 7.3
277 events, the variability in predicted average displacement at the fault is essentially indistinguishable.
278 Proper identification of the principal rupture trace is fundamental for the appropriate application
279 of our model. The assumption of $S_0 \ll S_{max}$ in this model, required to obtain the expression in
280 equation 7, underscores that our model is not appropriate to deduce the probability of large slip
281 on a secondary rupture. This is a minor limitation in the sense that, a second rupture hosting a
282 large slip is likely to be identified as an additional principal fault trace. Examples of this kind of
283 categorization exist for the Ridgecrest mainshock and the El Mayor-Cucapah events (see figure A1
284 in the appendix), where multiple, parallel ruptures are classified as principal fault traces.

285 Even when the principal rupture trace has been properly localized, there remains a small knee in
286 the curve of $P(S > S_0)$ in the very near-fault region, inherited from parameter x_{fr} in the expression
287 that describes the distribution of rupture density (equation 2). x_{fr} captures the uncertainty in
288 the location of this primary rupture trace and is on the order of a few meters for the events with
289 high-resolution maps we use in this study. The uncertainty in the fault location is an important
290 parameter to consider in PFDHA frameworks (e.g. Chen and Petersen, 2019). We expect that the
291 uncertainty in the principal fault trace location for faults without recent surface ruptures should be,
292 at a minimum, comparable to the values of x_{fr} deduced from these datasets. Thus, we consider x_{fr}
293 a useful parameter to incorporate into our model, as it results in a more conservative, wider zone
294 of, high $P(S > S_0)$ near the fault.

295 The Landers, Hector Mine, Ridgecrest, and El Mayor-Cucapah earthquakes show similar rupture
296 distributions. The slopes (γ) or scaling exponents of rupture density that yield the probability of
297 finding a rupture at a given distance away from the fault overlap within error (Figure 2), though
298 the exponents for the Ridgecrest foreshock and mainshock are comparatively lower than those for
299 the other events. We suspect the gentler slope of the Ridgecrest events partly results from the
300 inclusion of far-field features mapped as simplified lines based on geodetic observations, and from
301 the more thorough far-field coverage during the field mapping. The variation of rupture densities at
302 distances beyond 3 kilometers away from the main rupture likely results from variable mapping extent
303 (e.g. far-field coverage is not complete for each event), where the more complete far-field mapping
304 during the Ridgecrest events contributes to the more gentle scaling exponent in those distributions.
305 Incomplete far field map coverage is accounted for in our uncertainties and reflected in the increase
306 in uncertainty in our model with fault-perpendicular distance seen in Figure 7 (bottom).

307 An important consideration regarding our model uncertainties is that the posterior distributions
308 shown in Figures 3 and 2 only represent how well the models (equations 2 and 3) fit the spatial
309 distributions of rupture density and average displacement. These distributions omit the epistemic
310 uncertainty carried by these rupture maps and displacement measurements, which is associated
311 with variability in mapping completeness throughout, as well as in individual mapper decisions
312 when deciding where to place ruptures. The displacement distributions are also affected by the
313 individual location errors for each displacement measurement. We expect larger location errors
314 in the displacement measurements from the Landers and Hector Mine events, which predate the
315 relaxation of selective availability for GPS locations.

316 The epistemic uncertainties in these models could be largely mitigated through the data collection
317 process in future surface-rupturing earthquakes. In the case of the rupture distributions, even
318 coverage of the area surrounding the fault should largely reduce the far-field variability in the

319 distributions. For the displacements, more careful documentation of the complete displacement
320 range within the fault zone, without bias toward larger displacements, is necessary. This could be
321 achieved through even sampling of displacement measurements along the principal rupture zones.
322 In addition, careful documentation of the direction of displacement and separation of horizontal and
323 vertical components would enable an expansion of this model to include displacement direction, an
324 important component of assessing rupture hazard to engineered structures.
325 The characteristics of the events considered in this study make our model suitable for application
326 to other faults in immature fault zones (< 25 km of cumulative displacement) where large amounts
327 of distributed deformation are expected, in landscapes dominated by extensive sediment cover. Our
328 framework may not be appropriate for more mature fault zones with a higher degree of strain
329 localization (Dolan and Haravitch, 2014). Because the bulk of the surface ruptures we analyze
330 occurred in sediment, the application of this model for events predominantly in bedrock remains to
331 be tested. Last, events with substantial blind faulting cause largely different distributed deformation
332 patterns at the surface (e.g. Koehler et al., 2020), and therefore may not be well described by the
333 model proposed here, which requires a principal fault trace to be distinguishable.

334 Conclusions

335 Using detailed rupture maps from the Ridgecrest, Landers, Hector Mine, and El Mayor-Cucapah
336 earthquakes in southern California and northern Mexico, we develop a framework for PFDHA that
337 estimates the probability of finding a rupture with a displacement exceeding a threshold S_0 , located
338 at a given distance away from a principal fault trace. This model may be best applied to assess
339 rupture hazard for infrastructure in the near-field region (< 3 km) of immature faults (< 25 km of
340 cumulative displacement) where widespread secondary fault ruptures are expected, such as in the
341 Eastern California Shear Zone or the Walker Lake Belt of the western United States.

342 Acknowledgments

343 We thank Valère Lambert, Emily Brodsky, Kélian Dascher-Cousineau, and Magali Billen for discus-
344 sions that improved this work. We are grateful to Chris Madugo for suggestions that enhanced the
345 applicability of this model and to Alex Sarmiento for her help in navigating the FDHI database. This
346 research was made possible largely with support from a PG&E research award. Rodriguez Padilla
347 acknowledges support from NASA FINESST award 80NSSC21K1634. This is SCEC Contribution
348 No. 11869.

349 Data and resources

350 The rupture maps are available from the FDHI rupture database appendix <https://www.risksciences.ucla.edu/girs-reports/2021/08> (last accessed May 2022). The scripts used to generate the anal-
351 ysis in this paper and the Jupyter Notebook for end-users to work with our PFDHA framework are
352 available from https://github.com/absrp/strike_slip_PFDHA_model.
353

354 References

- 355 1. Antoine, S. L., Klinger, Y., Delorme, A., Wang, K., Bürgmann, R., & Gold, R. D. (2021).
356 Diffuse deformation and surface faulting distribution from submetric image correlation along

- 357 the 2019 Ridgecrest, California, ruptures. *Bull. Seismol. Soc. Am.*, (5), 2275-2302.
- 358 2. Baize, S., Azuma, T., Champenois, J., Cinti, F., Civico, R., Costa, C., ... & Schwartz, D.
359 (2017, November). Towards a unified and worldwide database of surface ruptures (SURE) for
360 Fault Displacement Hazard Analyses. In *Proceedings of the 8th International INQUA Meeting*
361 *on Paleoseismology, Active Tectonics and Archeoseismology (PATA)*, Blenheim, New Zealand
362 (pp. 13-16).
- 363 3. Baize, S., Nurminen, F., Sarmiento, A., Dawson, T., Takao, M., Scotti, O., ... & Villamor, P.
364 (2020). A worldwide and unified database of surface ruptures (SURE) for fault displacement
365 hazard analyses. *Seismological Research Letters*, 91(1), 499-520.
- 366 4. Brengman, C. M., Barnhart, W. D., Mankin, E. H., & Miller, C. N. (2019). Earthquake-scaling
367 relationships from geodetically derived slip distributions. *Bulletin of the Seismological Society*
368 *of America*, 109(5), 1701-1715.
- 369 5. Chen, T., Akciz, S. O., Hudnut, K. W., Zhang, D. Z., & Stock, J. M. (2015). Fault-
370 Slip Distribution of the 1999 M w 7.1 Hector Mine Earthquake, California, Estimated from
371 Postearthquake Airborne LiDAR Data. *Bulletin of the Seismological Society of America*,
372 105(2A), 776-790.
- 373 6. Chen, R., & Petersen, M. D. (2019). Improved implementation of rupture location uncertainty
374 in fault displacement hazard assessment. *Bulletin of the Seismological Society of America*,
375 109(5), 2132-2137.
- 376 7. Dolan, J. F., & Haravitch, B. D. (2014). How well do surface slip measurements track slip
377 at depth in large strike-slip earthquakes? The importance of fault structural maturity in
378 controlling on-fault slip versus off-fault surface deformation. *Earth and Planetary Science*
379 *Letters*, 388, 38-47.
- 380 8. DuRoss, C. B., Gold, R. D., Dawson, T. E., Scharer, K. M., Kendrick, K. J., Akciz, S. O., ... &
381 Zinke, R. (2020). Surface displacement distributions for the July 2019 Ridgecrest, California,
382 earthquake ruptures. *Bulletin of the Seismological Society of America*, 110(4), 1400-1418.
- 383 9. Fletcher, J. M., Teran, O. J., Rockwell, T. K., Oskin, M. E., Hudnut, K. W., Mueller, K.
384 J., ... & González-García, J. (2014). Assembly of a large earthquake from a complex fault
385 system: Surface rupture kinematics of the 4 April 2010 El Mayor-Cucapah (Mexico) Mw 7.2
386 earthquake. *Geosphere*, 10(4), 797-827.
- 387 10. Hart, E. 1994. Calico Fault and Adjacent 1992 Surface Ruptures near Newberry Springs, San
388 Bernardino County. California Division of Mines and Geology Fault Evaluation Report, 238,
389 California Geological Survey CD 2002-02.
- 390 11. Hudnut, K. W., Borsa, A., Glennie, C., & Minster, J. B. (2002). High-resolution topography
391 along surface rupture of the 16 October 1999 Hector Mine, California, earthquake (M w 7.1)
392 from airborne laser swath mapping. *Bulletin of the Seismological Society of America*, 92(4),
393 1570-1576.
- 394 12. Hudnut, K. W., Brooks, B. A., Scharer, K., Hernandez, J. L., Dawson, T. E., Oskin, M. E.,
395 ... & Sorhus, S. (2020). Airborne lidar and electro-optical imagery along surface ruptures of
396 the 2019 Ridgecrest earthquake sequence, southern California. *Seismological Research Letters*,
397 91(4), 2096-2107.

- 398 13. Koehler, R. D., Dee, S., Elliott, A., Hatem, A., Pickering, A., Pierce, I., & Seitz, G. (2021).
399 Field response and surface-rupture characteristics of the 2020 M 6.5 Monte Cristo range earth-
400 quake, Central Walker Lane, Nevada. *Seismological Research Letters*, 92(2A), 823-839.
- 401 14. Lazarte, C. A., Bray, J. D., Johnson, A. M., & Lemmer, R. E. (1994). Surface breakage of the
402 1992 Landers earthquake and its effects on structures. *Bulletin of the Seismological Society of*
403 *America*, 84(3), 547-561.
- 404 15. Mattioli, G. S., Phillips, D. A., Hodgkinson, K. M., Walls, C., Mencin, D. J., Bartel, B. A.,
405 ... & Zaino, A. (2020). The GAGE data and field response to the 2019 Ridgecrest earthquake
406 sequence. *Seismological Research Letters*, 91(4), 2075-2086.
- 407 16. Milliner, C. W., Dolan, J. F., Hollingsworth, J., Leprince, S., Ayoub, F., & Sammis, C. G.
408 (2015). Quantifying near-field and off-fault deformation patterns of the 1992 Mw 7.3 Landers
409 earthquake. *Geochemistry, Geophysics, Geosystems*, 16(5), 1577-1598.
- 410 17. Milliner, C. W. D., Dolan, J. F., Hollingsworth, J., Leprince, S., & Ayoub, F. (2016). Com-
411 parison of coseismic near-field and off-fault surface deformation patterns of the 1992 Mw 7.3
412 Landers and 1999 Mw 7.1 Hector Mine earthquakes: Implications for controls on the distribu-
413 tion of surface strain. *Geophysical Research Letters*, 43(19), 10-115.
- 414 18. Milliner, C., & Donnellan, A. (2020). Using daily observations from Planet Labs satellite
415 imagery to separate the surface deformation between the 4 July Mw 6.4 foreshock and 5 July
416 Mw 7.1 mainshock during the 2019 Ridgecrest earthquake sequence. *Seismological Research*
417 *Letters*, 91(4), 1986-1997.
- 418 19. Milliner, C., Donnellan, A., Aati, S., Avouac, J. P., Zinke, R., Dolan, J. F., ... & Bürgmann, R.
419 (2021). Bookshelf kinematics and the effect of dilatation on fault zone inelastic deformation:
420 Examples from optical image correlation measurements of the 2019 Ridgecrest earthquake
421 sequence. *Journal of Geophysical Research: Solid Earth*, 126(3), e2020JB020551.
- 422 20. Moss, R. E. S., & Ross, Z. E. (2011). Probabilistic fault displacement hazard analysis for
423 reverse faults. *Bulletin of the Seismological Society of America*, 101(4), 1542-1553.
- 424 21. Nurminen, F., Boncio, P., Visini, F., Pace, B., Valentini, A., Baize, S., & Scotti, O. (2020).
425 Probability of occurrence and displacement regression of distributed surface rupturing for
426 reverse earthquakes. *Frontiers in Earth Science*, 8, 581605.
- 427 22. Petersen, M. D., Dawson, T. E., Chen, R., Cao, T., Wills, C. J., Schwartz, D. P., & Frankel,
428 A. D. (2011). Fault displacement hazard for strike-slip faults. *Bulletin of the Seismological*
429 *Society of America*, 101(2), 805-825.
- 430 23. Ponti, D. J., Blair, J. L., Rosa, C. M., Thomas, K., Pickering, A. J., Akciz, S., ... & Zinke,
431 R. (2020). Documentation of surface fault rupture and ground-deformation features produced
432 by the 4 and 5 July 2019 Mw 6.4 and Mw 7.1 Ridgecrest earthquake sequence. *Seismological*
433 *Research Letters*, 91(5), 2942-2959.
- 434 24. Powers, P. M., & Jordan, T. H. (2010). Distribution of seismicity across strike-slip faults in
435 California. *Journal of Geophysical Research: Solid Earth*, 115(B5).
- 436 25. Rodriguez Padilla, A. M., Quintana, M. A., Prado, R. M., Aguilar, B. J., Shea, T. A., Oskin,
437 M. E., & Garcia, L. (2022a). Near-Field High-Resolution Maps of the Ridgecrest Earthquakes
438 from Aerial Imagery. *Seismological Society of America*, 93(1), 494-499.

- 439 26. Rodriguez Padilla, A. M., Oskin, M. E., Milliner, C. W., & Plesch, A. (2022b). Accrual of
440 widespread rock damage from the 2019 Ridgecrest earthquakes. *Nature Geoscience*, 15(3),
441 222-226.
- 442 27. Sarmiento, A., Madugo, D., Bozorgnia, Y., Shen, A., Mazzoni, S., Lavrentiadis, G., Dawson,
443 T., Madugo, C., Kottke, A., Thompson, S., Baize, S., Milliner, C., Nurminen, F., Boncio, P.,
444 and Visini, F. (2021). Fault Displacement Hazard Initiative Database, UCLA B. John Garrick
445 Institute for the Risk Sciences, Report GIRS-2021-08, doi: 10.34948/N36P48.
- 446 28. Sieh, K., Jones, L., Hauksson, E., Hudnut, K., Eberhart-Phillips, D., Heaton, T., ... &
447 Zachariasen, J. (1993). Near-field investigations of the Landers earthquake sequence, April
448 to July 1992. *Science*, 260(5105), 171-176.
- 449 29. Teran, O. J., Fletcher, J. M., Oskin, M. E., Rockwell, T. K., Hudnut, K. W., Spelz, R. M., ... &
450 Morelan, A. E. (2015). Geologic and structural controls on rupture zone fabric: A field-based
451 study of the 2010 Mw 7.2 El Mayor–Cucapah earthquake surface rupture. *Geosphere*, 11(3),
452 899-920.
- 453 30. Treiman, J. A., Kendrick, K. J., Bryant, W. A., Rockwell, T. K., & McGill, S. F. (2002).
454 Primary surface rupture associated with the M w 7.1 16 October 1999 Hector mine earthquake,
455 San Bernardino County, California. *Bulletin of the Seismological Society of America*, 92(4),
456 1171-1191.
- 457 31. Wang, Y., & Goulet, C. (2021). Validation of fault displacements from dynamic rupture simu-
458 lations against the observations from the 1992 landers earthquake. *Bulletin of the Seismological*
459 *Society of America*, 111(5), 2574-2594.
- 460 32. Wells, D. L., & Coppersmith, K. J. (1994). New empirical relationships among magnitude,
461 rupture length, rupture width, rupture area, and surface displacement. *Bulletin of the seismo-*
462 *logical Society of America*, 84(4), 974-1002.
- 463 33. Xu, X., Sandwell, D. T., & Smith-Konter, B. (2020). Coseismic displacements and surface
464 ruptures from Sentinel-1 InSAR: 2019 Ridgecrest earthquakes. *Seismological Research Letters*,
465 91(4), 1979-1985.
- 466 34. Youngs, R. R., Arabasz, W. J., Anderson, R. E., Ramelli, A. R., Ake, J. P., Slemmons, D. B.,
467 ... & Toro, G. R. (2003). A methodology for probabilistic fault displacement hazard analysis
468 (PFDHA). *Earthquake spectra*, 19(1), 191-219.

469 **2 Figures**

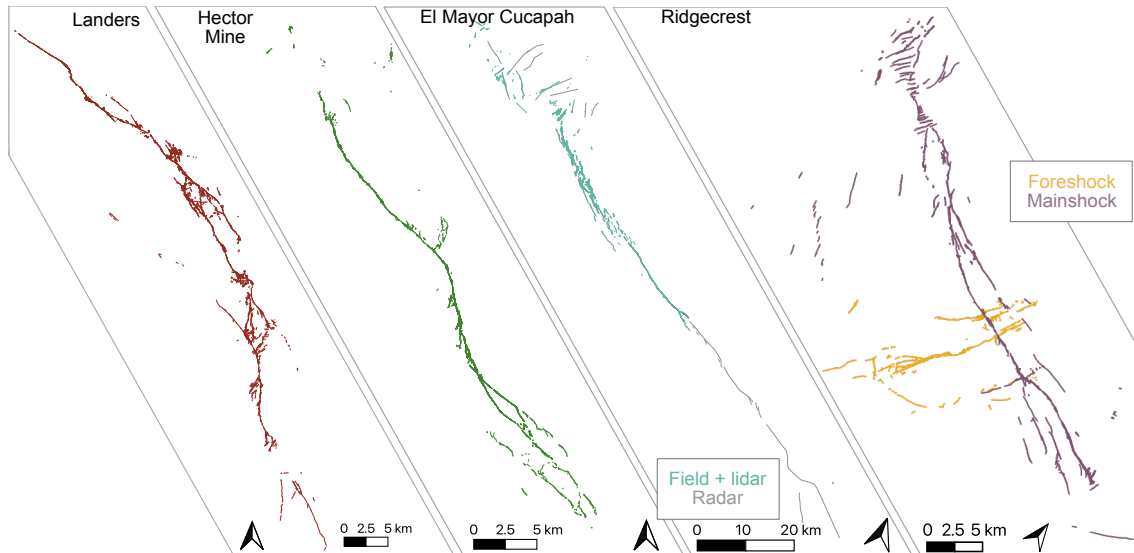


Figure 1: Surface rupture maps from the Landers, Hector Mine, El Mayor-Cucapah, and Ridgecrest earthquakes from the Fault Displacement Hazard Initiative database (Sarmiento et al., 2021). The gray lines in the El Mayor-Cucapah rupture are simplified traces mapped from radar data and excluded in this study. The turquoise lines were mapped from field and lidar data and included here. The purple lines in the Ridgecrest map represent mainshock rupture map and the orange lines represent the foreshock rupture map.

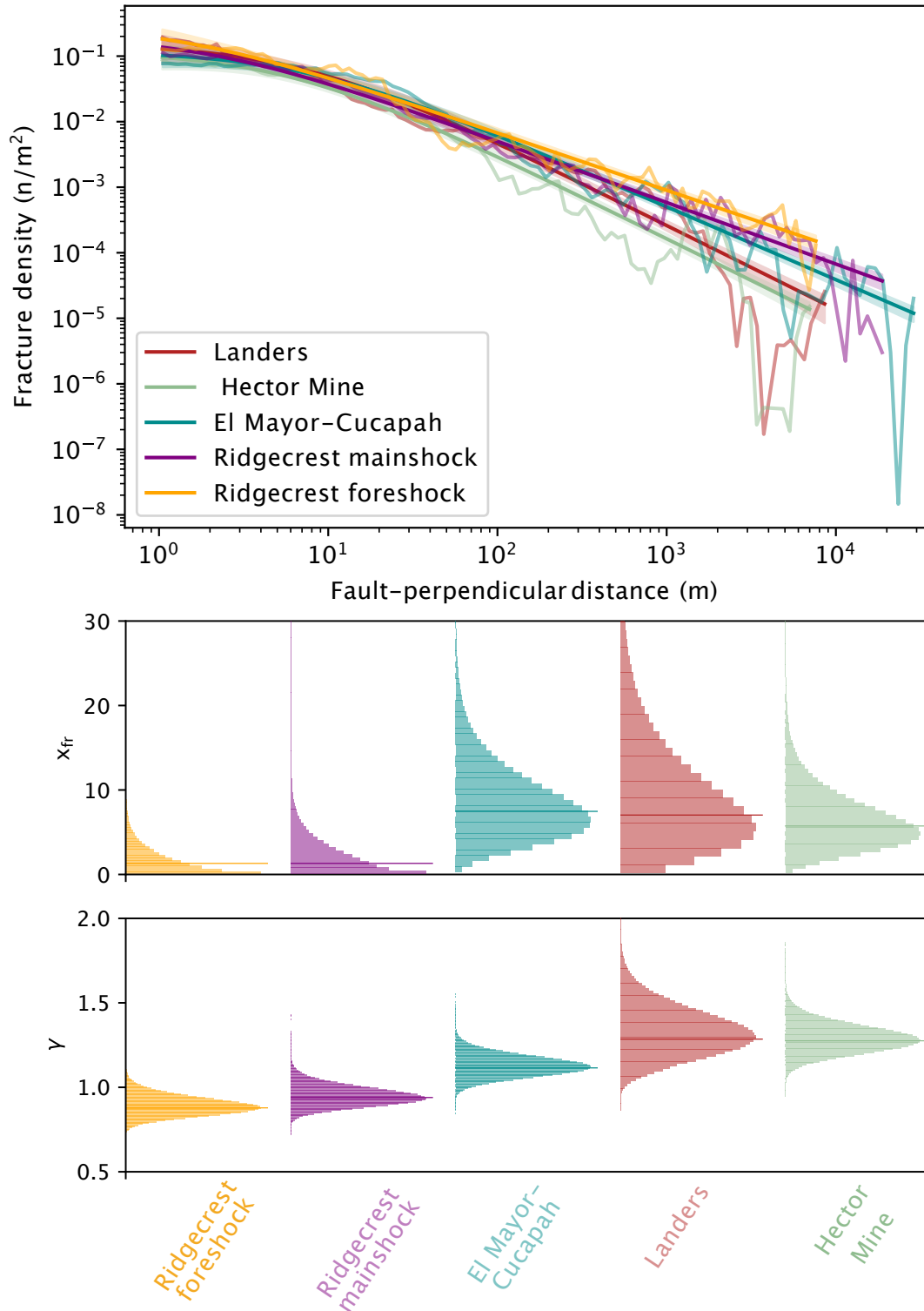


Figure 2: Rupture density distribution for the Landers, Hector Mine, El Mayor-Cucapah, and Ridgecrest earthquakes. The Ridgecrest foreshock and mainshock are shown as separate events. The shaded region represents the fits within one standard deviation of the maximum likelihood fit, shown as the bold line, fit using 2. The bottom panel shows the distribution of posterior values for γ , the scaling exponent of the density-distribution, and x_{fr} , the uncertainty on the location of the principal fault trace.

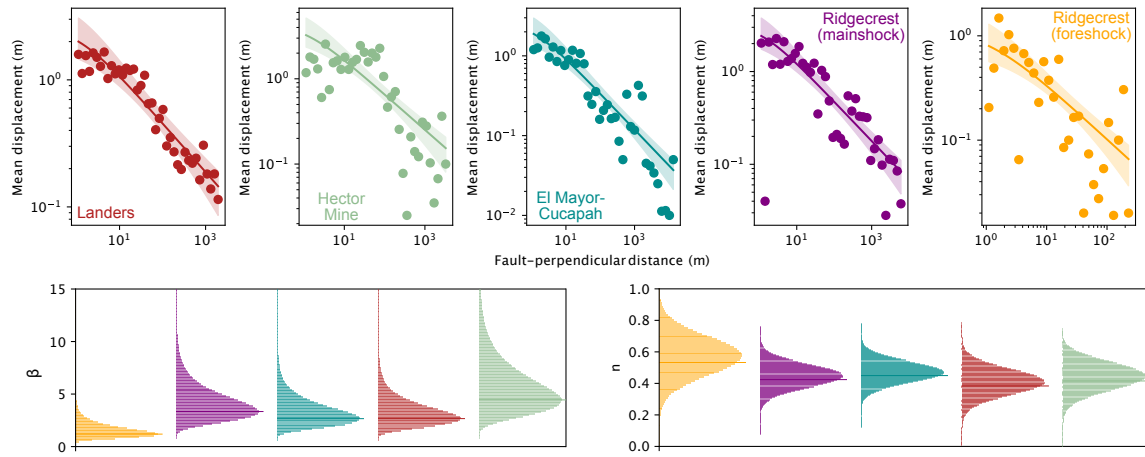


Figure 3: Distribution of average displacement measured in the field for the Landers, Hector Mine, El Mayor-Cucapah, and Ridgecrest earthquakes. The scattered dots on the top plot represent the field displacement data for each event from the FDHI database (Sarmiento et al., 2021). The solid lines represent the maximum likelihood fits to the distribution and the shaded area shows the 1σ posterior distribution from an MCMC fit. The bottom panels show the posterior distributions of β and n , fit using equation 3.

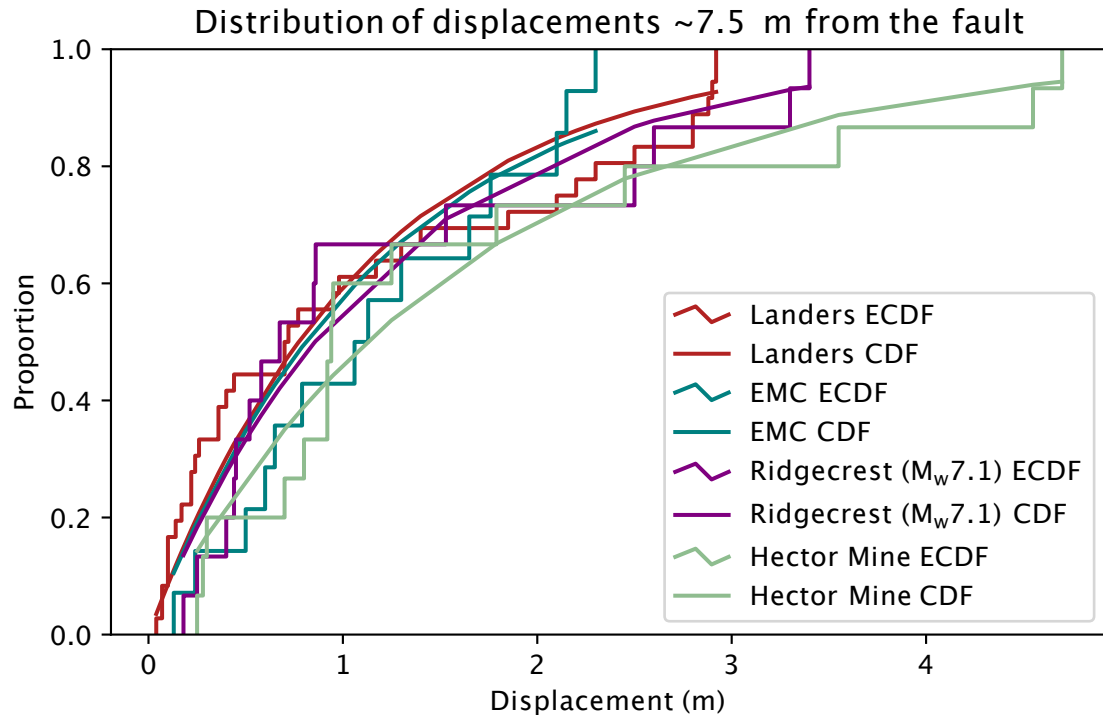


Figure 4: Empirical cumulative distribution function of the displacements ~ 7.5 meters away from the fault for the Landers, Hector Mine, El Mayor-Cucapah, and Ridgecrest earthquakes. Note that we omit the Ridgecrest foreshock from this plot for clarity because the displacements are much smaller given the smaller magnitude. The cumulative distribution functions fit from the mean of the empirical data are plotted on top.

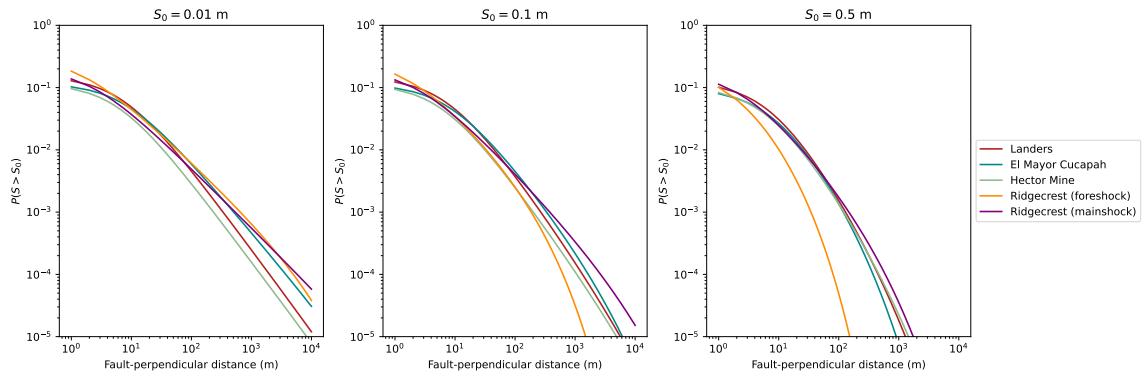


Figure 5: PFDHA model expressing the probability of finding a rupture hosting a displacement that exceeds threshold S_0 for the Landers, Hector Mine, El Mayor-Cucapah, and Ridgecrest earthquakes. The models are generated using equation 8. We show models for $S_0 = 0.01$ m, 0.1 m, and 0.5 m.

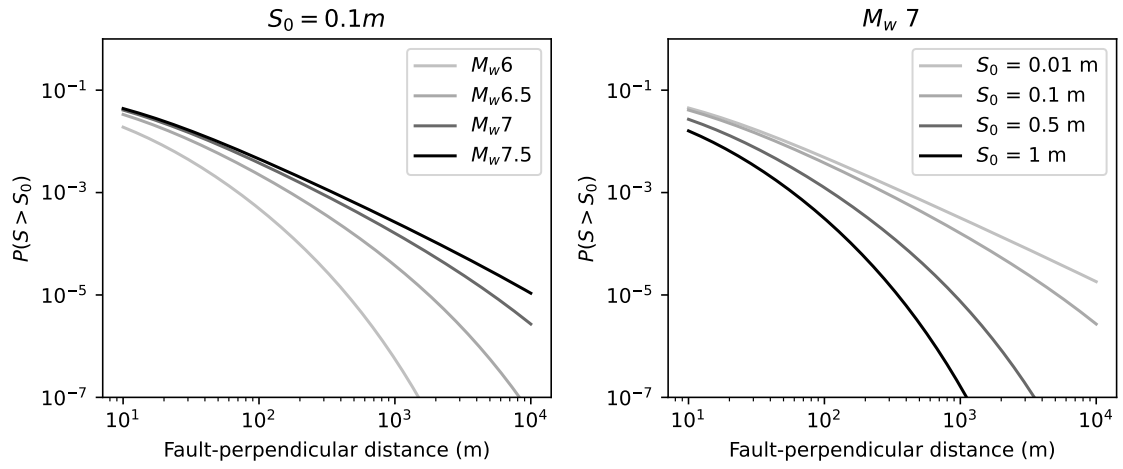


Figure 6: PFDHA model expressing the probability of finding a rupture hosting a displacement that exceeds threshold S_0 for a surface-rupturing strike-slip earthquake. The models are generated using equation 8. On the left, we show models for $M_w = 5, 6,$ and 7 , where $S_0 = 0.1 m$. On the right, we show models for $S_0 = 0.1, 0.5,$ and 1 meter, for an $M_w 7$ event.

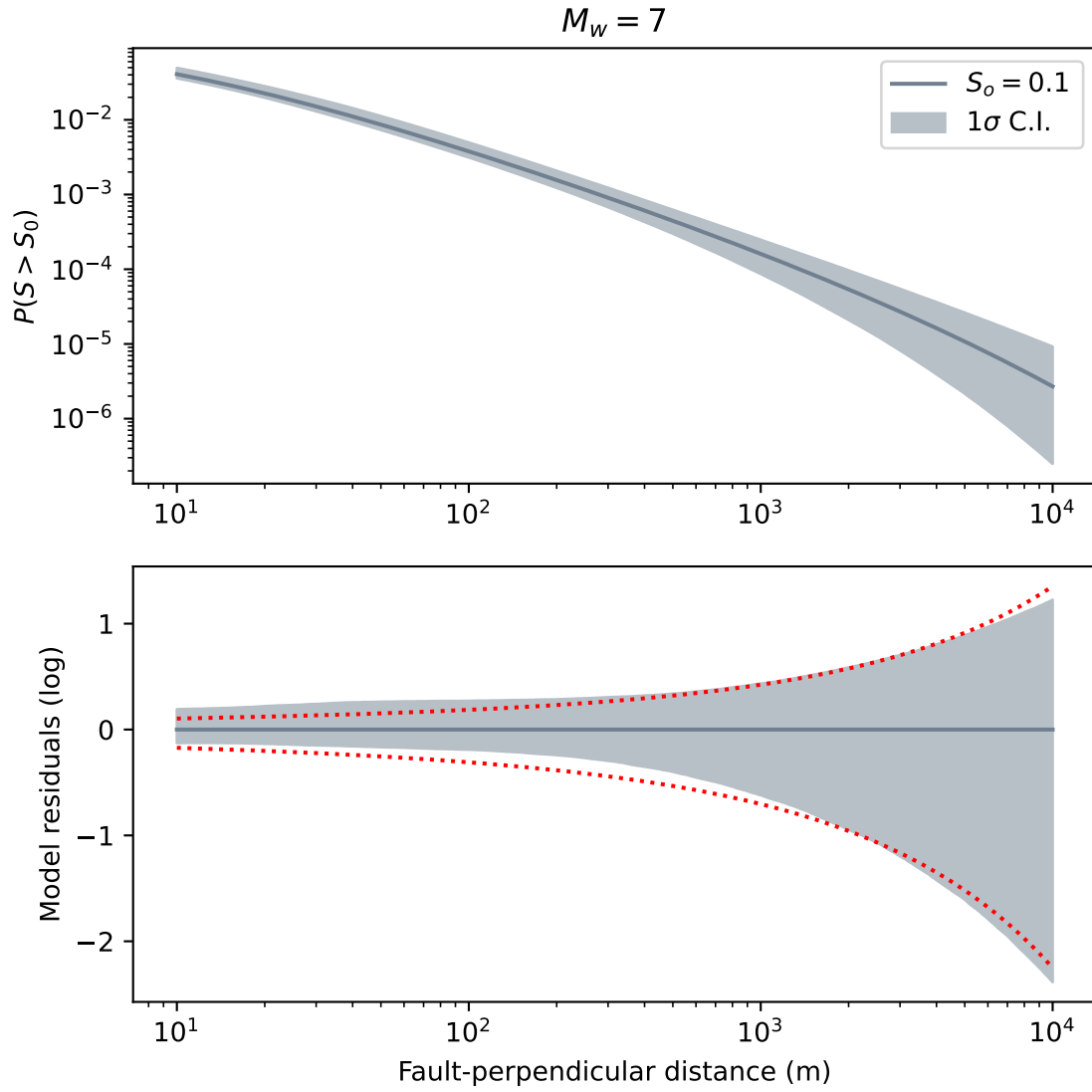


Figure 7: Top: PFDHA model expressing the probability of finding a rupture hosting a displacement that exceeds threshold $S_0 = 0.1$ m for a surface-rupturing strike-slip earthquake of M_w 7. The model is generated using equation 8. The shading represents the 1σ confidence intervals. The solid line represents the best-fit model. Bottom: Model residuals (log). The dotted red line represents the fit of equation 10 to the logarithmic of the residuals.

Parameter	Landers	Hector Mine	El Mayor-Cucapah	Ridgecrest (foreshock)	Ridgecrest (mainshock)	General model
v_0	0.15	0.28	0.12	0.31	0.20	0.13
x_{fr} (meters)	7.0	2.0	7.5	1.3	2.0	6.7
γ	1.3	1.2	1.1	0.9	0.9	1.2
β (meters)	2.7	4.4	2.7	1.2	3.3	$\beta(M_w)$
n	0.38	0.42	0.45	0.53	0.42	0.44

470 **Table 1.** Distribution of best-fit parameters for each event and the general model in equation 8.

471 Appendix

472 A Supplementary figures

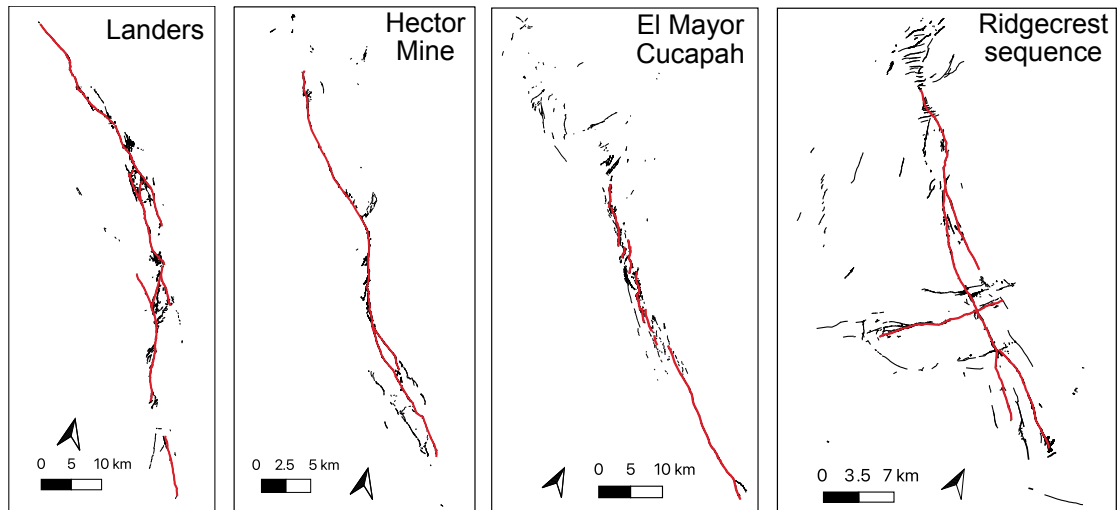


Figure A1: Secondary ruptures (black) and simplified principal rupture trace (red) for each event considered in this study.

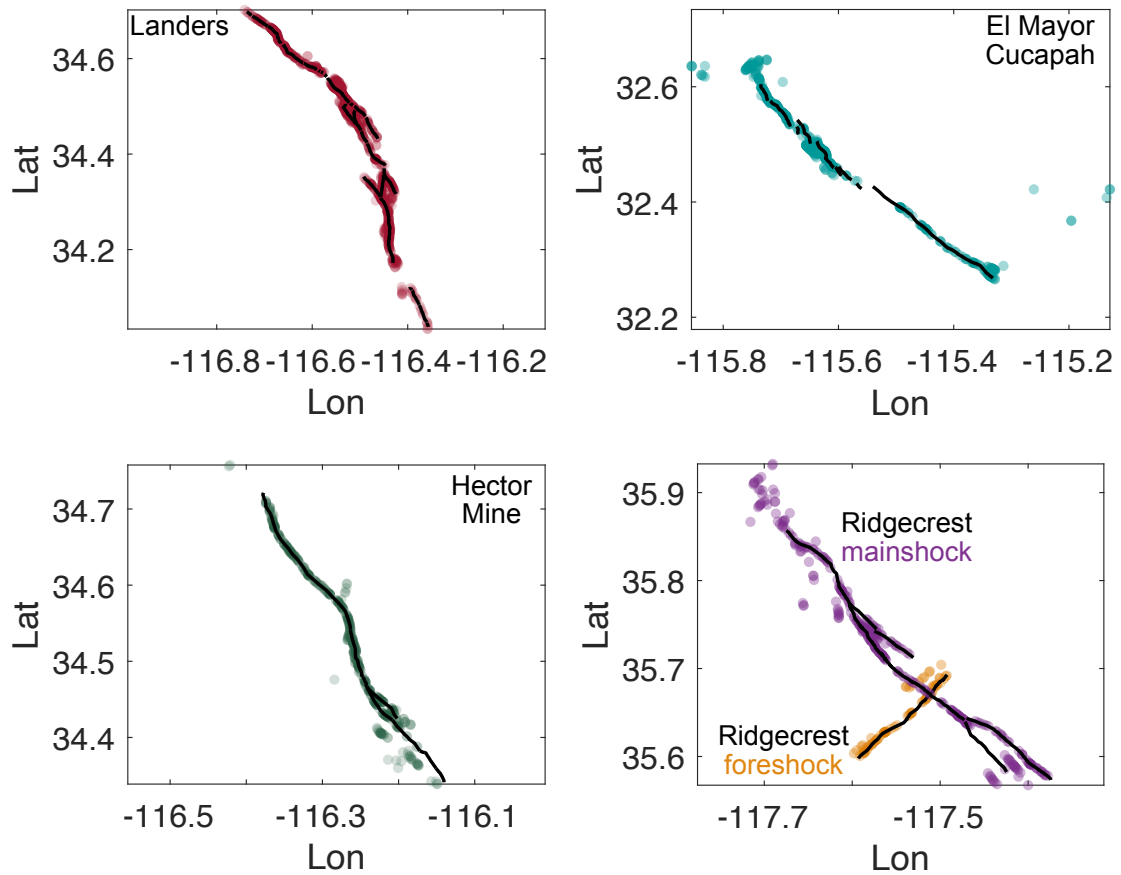


Figure A2: Displacement data from the Landers (red), Hector Mine (green), El Mayor-Cucapah (teal), and Ridgecrest earthquakes (foreshock in orange and mainshock in purple) plotted over the principal rupture trace of each event. The displacement data is sourced from the Fault Displacement Hazard Initiative database (Sarmiento et al., 2021) and we only consider measurements collected in the field. The principal rupture traces are roughly simplified from the ruptures classified as primary in the FDHI database (see figure A1) in the appendix.

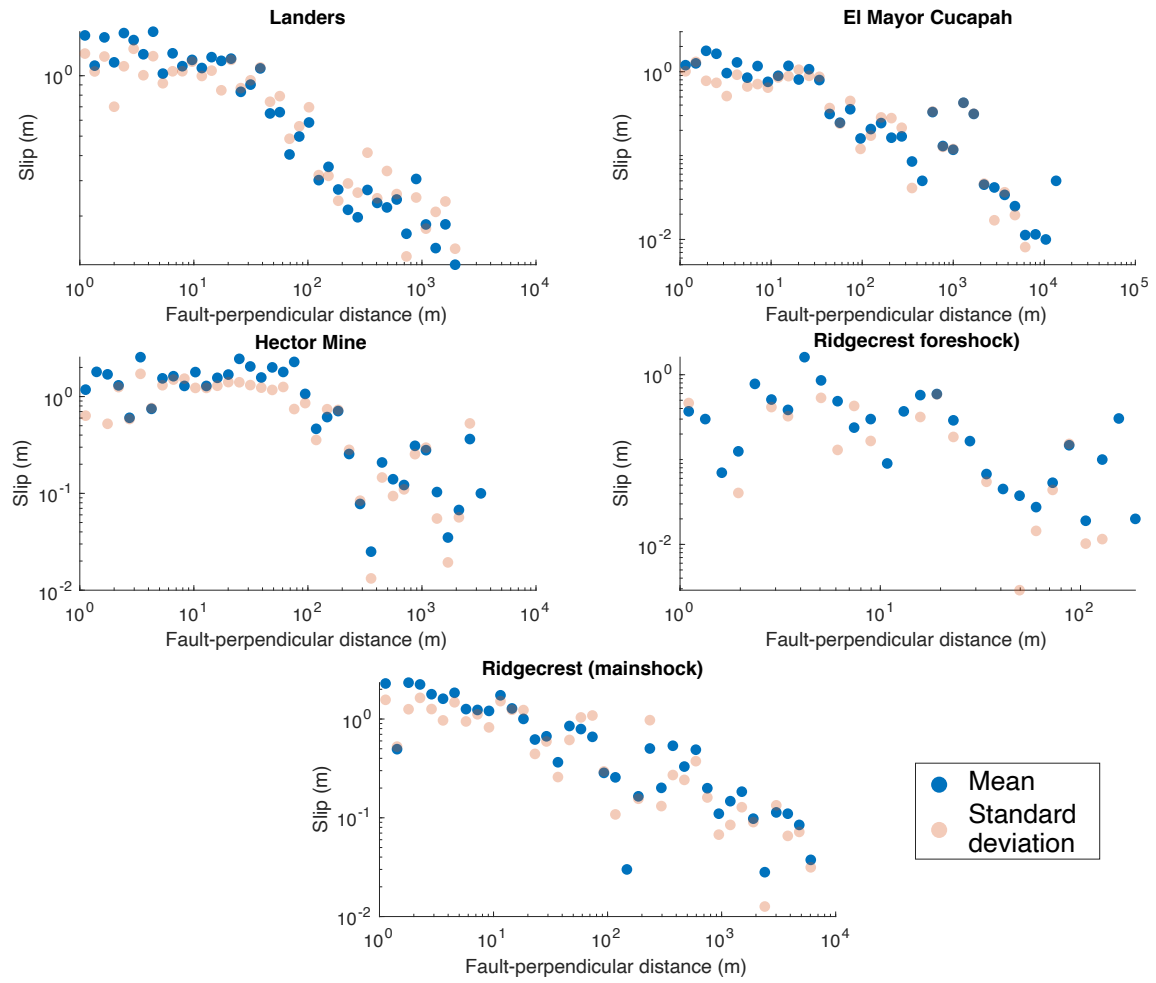


Figure A3: Mean (blue) and standard deviation (pink) of slip with fault-perpendicular distance for the Landers, Hector Mine, El Mayor-Cucapah, and Ridgecrest earthquakes. The consistent correlation of the mean and the standard deviation suggests the displacements are exponentially distributed within each distance bin.

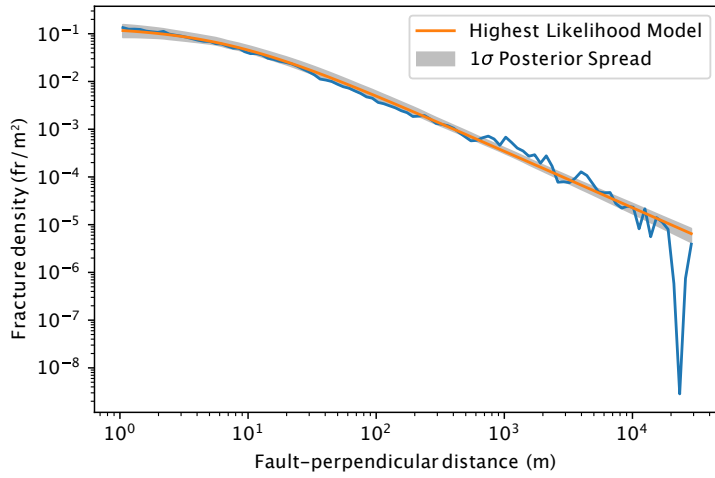


Figure A4: General model for the decay of rupture density with fault-perpendicular distance generated from combining the secondary rupture maps from the Landers, Hector Mine, El Mayor-Cucapah, and Ridgecrest earthquakes.

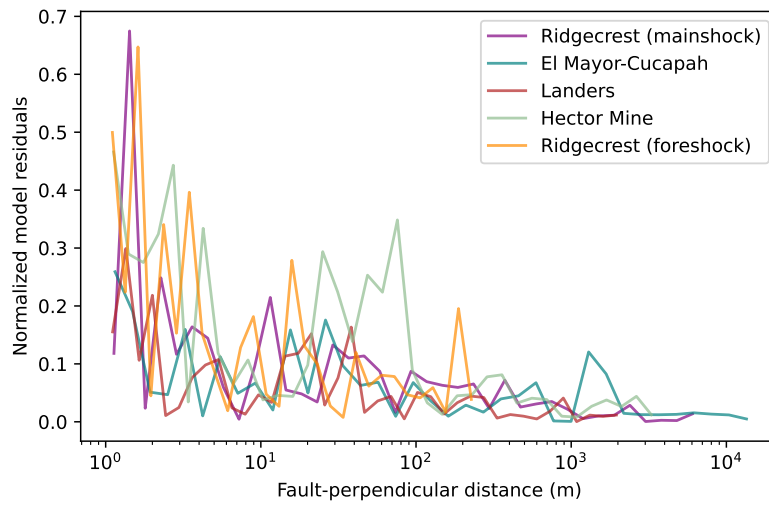


Figure A5: Model residuals from the fits of equation 3 to the field displacement data in the FDHI database for each event (figure 3). The residuals are normalized by the value of β for each event to account for the magnitude-dependence of displacement.

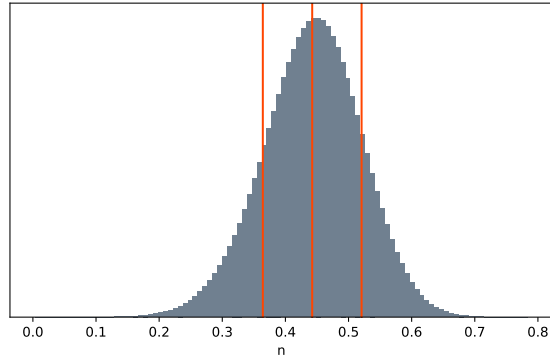


Figure A6: Concatenated posteriors for n in equations 3 and 8 from the Landers, Ridgecrest main-shock, and El Mayor-Cucapah event. Note that n is roughly normally distributed. The vertical red lines indicate the mean and data within one standard deviation of the mean.

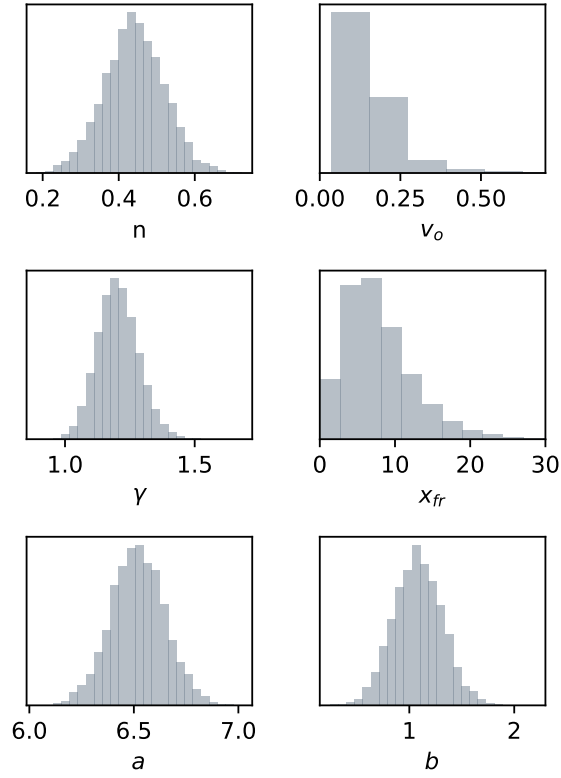


Figure A7: Distribution of parameters from equation 8. ν_o , x_{fr} , and γ are sampled from the posterior distributions of the fits in supplementary figure A4. n , a , and b are sampled from normal distributions where the mean and standard deviation are calculated in this study for n (figure A6 in the appendix) and in Brengman et al. (2019) for a and b .

473 **Supplementary methods**

474 We build on the method in Rodriguez Padilla et al. (2022b) to estimate the decay of rupture
475 density with fault-perpendicular distance for each event. We begin by discretizing every rupture
476 into 1m spaced points, to minimize the effect of mapper bias in rupture continuity. Next, we
477 measure the distance between each point and the nearest point on the main rupture. The principal
478 rupture is simplified for each event from the cracks defined as primary in the FDHI rupture database
479 (supplementary figure A1). We then log bin the distances into 100 bins, from 0 to the furthest rupture
480 from the main rupture, and count the number of rupture segments per bin. Last, we normalize each
481 bin by its size, and the entire decay by the total length of the principal fault. This produces the
482 decays shown in Figure 2.

483 We fit each decay with an affine-invariant ensemble sampler for Markov Chain Monte Carlo (Good-
484 man and Weare, 2010; Foreman-Mackay et al., 2013) to estimate the maximum likelihood parameters
485 for equation 2. As priors, we use uniformly distributed values of $\nu_o = (0, 3)$, $x_{fr} = (0, 100)$ meters,
486 and $\gamma = (0, 3)$. We assume that the error of $\nu(x)$ in each bin is Poisson-distributed, following the
487 method of Powers and Jordan (2010). We employ an ensemble of 200 walkers, which run for 100,000
488 iterations, following a 10,000-iteration burn-in period.

489 We follow a similar approach to estimate the decay of average displacement with fault-perpendicular
490 distance. We take the displacements from the FDHI database for each event and measure their
491 distance to the principal rupture trace (supplementary figure A1). We then log-bin the distances into
492 40 bins, from 0 to the furthest rupture from the main rupture, and calculate the average displacement
493 per bin. This produces the decays shown in Figure 3. We fit each decay with an affine-invariant
494 ensemble sampler for Markov Chain Monte Carlo (Goodman and Weare, 2010; Foreman-Mackay et
495 al., 2013) to estimate the maximum likelihood parameters for equation 3. As priors, we use uniformly
496 distributed values of $\beta = (0, 15)$ meters and $n = (0, 3)$. We employ an ensemble of 200 walkers, which
497 run for 100,000 iterations, following a 10,000-iteration burn-in period. Note that we fix $x_S = 1$ meter
498 in equation 3 because this provides a better model fit than letting x_S be a free parameter that is
499 fit with the ensemble sampler for MCMC and contributes to reducing uncertainty in the model fits.
500 We also tested values of $x_S = 10$ meters, with worse residuals, thus the choice of $x_S = 1$ meter.

501 **Supplemental references**

- 502 1. Foreman-Mackey, D., Hogg, D. W., Lang, D., & Goodman, J. (2013). emcee: the MCMC
503 hammer. *Publications of the Astronomical Society of the Pacific*, 125(925), 306.
- 504 2. Goodman, J., & Weare, J. (2010). Ensemble samplers with affine invariance. *Communications*
505 *in applied mathematics and computational science*, 5(1), 65-80.
- 506 3. Powers, P. M., & Jordan, T. H. (2010). Distribution of seismicity across strike-slip faults in
507 California. *Journal of Geophysical Research: Solid Earth*, 115(B5).